

## Article

# Driving towards Sustainability: Wireless Charging of Low-Speed Vehicles with PDM-Based Active Bridge Rectifiers

Yuvaraja Shanmugam <sup>1</sup>, Narayanamoorthi Rajamanickam <sup>1,\*</sup>, Roobaea Alroobaea <sup>2</sup> and Abdulkareem Afandi <sup>3,\*</sup>

<sup>1</sup> Wireless Charging Research Centre, Department of Electrical and Electronics Engineering, SRM Institute of Science and Technology, Chennai 603203, India; ys4557@srmist.edu.in

<sup>2</sup> Department of Computer Science, College of Computers and Information Technology, Taif University, P.O. Box 11099, Taif 21944, Saudi Arabia; r.robai@tu.edu.sa

<sup>3</sup> General Subject Department, University of Business and Technology, Jeddah 23435, Saudi Arabia

\* Correspondence: narayanr@srmist.edu.in (N.R.); a.afandi@ubt.edu.sa (A.A.)

**Abstract:** The surge in demand for eco-friendly transportation and electric vehicle (EV) charging infrastructure necessitates innovative solutions. This study proposed a novel approach to charging slow-moving vehicles, prioritizing efficiency and minimizing output pulsation. Central to the research is the development of a receiver-side power-regulated constant charging system, focusing on power regulation and maintaining consistent charging parameters. This system integrates a receiver-side pulse density-modulated active bridge rectifier, dynamically adjusting driving pulse density to regulate delivered power. Additionally, a receiver-side reconfigurable compensation network ensures constant current and voltage delivery to the charging device, eliminating the need for an additional D.C.-D.C. converter. A 3.3 kW charging structure employing a multi-leg inverter topology and energizing four ground-side transmitter pads exemplifies the proposed approach. The vertical air gap of charging pads is 150 mm, and the system achieves a maximal efficiency of 93.4%. This innovative strategy holds significant promise for advancing sustainable transportation infrastructure and meeting the evolving demands of the EV market.

**Keywords:** wireless charging; active bridge rectifier; dynamic wireless charging; pulse density modulation; multi-legged inverter



**Citation:** Shanmugam, Y.; Rajamanickam, N.; Alroobaea, R.; Afandi, A. Driving towards Sustainability: Wireless Charging of Low-Speed Vehicles with PDM-Based Active Bridge Rectifiers. *Sustainability* **2024**, *16*, 3810. <https://doi.org/10.3390/su16093810>

Academic Editors: Francesco Riganti-Fulginei and Michele Quercio

Received: 19 March 2024

Revised: 18 April 2024

Accepted: 25 April 2024

Published: 1 May 2024



**Copyright:** © 2024 by the authors. Licensee MDPI, Basel, Switzerland. This article is an open access article distributed under the terms and conditions of the Creative Commons Attribution (CC BY) license (<https://creativecommons.org/licenses/by/4.0/>).

## 1. Introduction

The market of electric vehicles (EVs) has experienced a remarkable surge in recent years [1]. EVs play a pivotal role in mitigating climate change, reducing air pollution, and promoting energy independence. As technical improvements continue and related costs fall, EVs are expected to become the primary mode of transportation in the decades to come. Their potential to contribute to environmental sustainability and energy security makes them a judicious investment for both private and commercial use [2,3]. As such, businesses and policymakers must accord paramount importance to the adoption of EVs to achieve long-term sustainability goals and reduce the emission of pollutant gases. Figure 1a shows the expansion of the EV sector in various countries. EV usage is encouraged by the effectiveness of a widely dispersed network of charging facilities in alleviating concerns regarding power depletion during extended drives. Easy access to charging points makes owning an EV a seamless experience, further driving adoption [4,5]. It is imperative to prioritize the requisite infrastructure to support EVs and ensure that charging stations are conveniently located and easily accessible [6,7].

Significant EV charging methods include swapping batteries, and inductive, and conductive charging [8,9]. Level 1 (1- $\phi$  A.C., 120 V input), Level 2 (1- $\phi$  A.C., 240 V input), and D.C. Fast charging (3- $\phi$  A.C. input) is a different type of wired charging that is classified based on battery charging rate [10,11]. Wired charging faces challenges with charging

infrastructure compatibility and reliability due to differing standards, human dependence on the charging process, and the wear and tear of bulk cables, necessitating costly maintenance. By replacing a depleted battery with a completely charged one in an instant, battery swapping [12,13] helps users minimize downtime. Standardization, logistics, infrastructure investment, compatibility, technology obsolescence, weight and space restrictions, and restricted applicability to specific types of EVs are some of the problems associated with its adoption. It also minimizes concerns about battery deterioration and tackles infrastructure-related charging difficulties. Standardization is challenging, though, because different EV manufacturers utilize varying battery types, sizes, and mounting techniques. It can also be difficult to maintain a fleet of batteries, monitor their status, and make sure that swapping stations have enough supply of fully charged batteries [14].

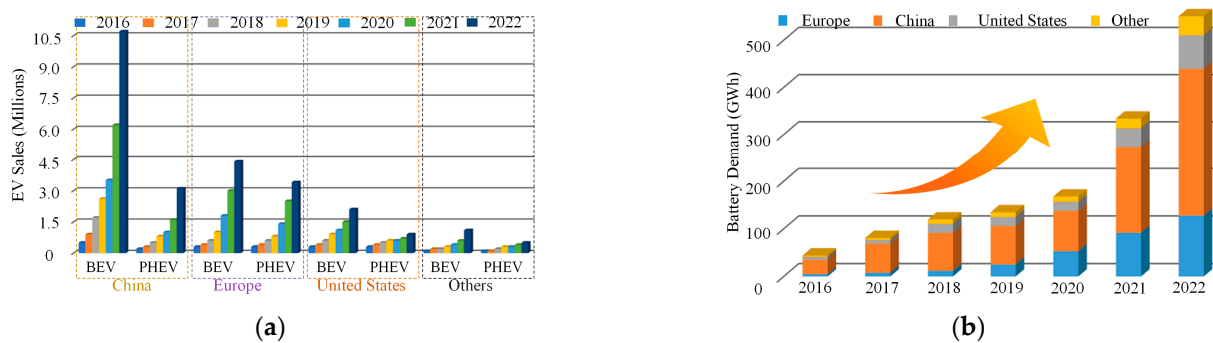


**Figure 1.** (a) EV sales data by country. (b) Battery requirements by country [1].

The removal of physical connectors improves the efficiency of wireless charging by minimizing the risk of electrical shock and deterioration for both the infrastructure for charging facilities and the EVs [15,16]. Automatic charging begins the moment a compatible EV parks over the wireless charging pad, rendering it convenient to use and efficient. The several existing technologies for wireless charging include radio frequency, capacitive, inductive, and resonant inductive. Resonant inductive wireless charging utilizes resonant induction to transfer electrical energy between ground assembly and vehicle assembly wirelessly. It allows for charging over longer distances than typical inductive charging. The system comprises a ground assembly with a transmitter pad and a vehicle assembly with a receiver pad [17,18]. These pads resonate at the resonance frequency, producing an electromagnetic field in the pads and causing an A.C. to be induced in the pad. In addition, the wireless charging techniques may be categorized as stationary or dynamic depending on the velocity of the vehicle [19]. Stationary wireless charging is suitable for vehicles that have been parked for an extended length of time, is simple to integrate into existing infrastructure, and is appropriate for personal and fleet vehicles with predictable usage patterns. Dynamic wireless charging (DWC) provides continuous charging, extends EV driving range, and is beneficial for high-usage scenarios such as electric buses and taxis [20]. Moreover, it can diminish the capacity of the EV's internal battery, resulting in a reduction in both the weight and price of the vehicle. Figure 1b depicts the battery demand of the various countries over the period. The concept of the DWC system is the integration of charging tracks into the road surface at predetermined intervals. These charging elements utilize resonant inductive coupling to ensure power transfer efficiency [21].

A continuous charging process occurs when the EV is in momentum on the electrically powered track, which extends its range and reduces its dependence on cumbersome onboard batteries [22]. Communication protocols and control systems oversee the charging process, encompassing the monitoring of the battery status, power regulation, and guaranteeing safety [23]. Figure 2 represents the DWC system's basic representation. Vehicle-side and ground-side are the two assemblies in DWC infrastructure.

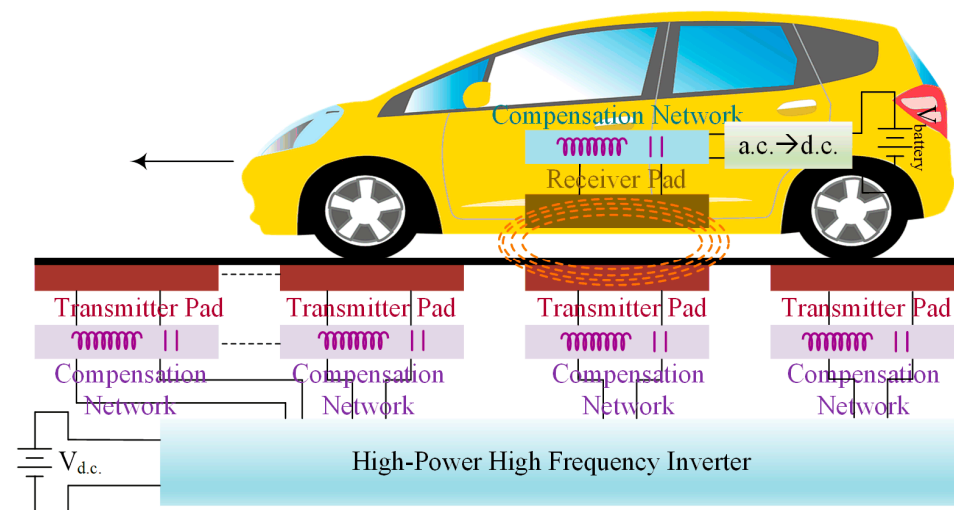


**Figure 2.** Representation of quasi-dynamic wireless charging system.

The DWC system consists of two primary components: the ground side, which includes a transmitter pad, compensation network, high-power high-frequency inverter, and sensors; and the vehicle side, which includes a receiver pad, resonant network, high-power high-frequency converter, sensors, and storage system. A proficient controller oversees the charging procedure and ensures optimal power transfer [24]. Charging couplers play a crucial role in the DWC system. Several types of couplers are often used [25]. These structures may be classified based on the direction of flux they produce [26]. Non-polarized pad structures are typically circular, rectangular, hexagonal, or square in shape and are capable of generating either horizontal or vertical flux. In contrast, polarized pads such as DD (Double-D shape), DDQ (DD with Quadrature), BP (Bipolar), TP (Tripolar), and QP (Quadrapule) can produce magnetic flux in both horizontal and vertical orientations [27]. The utilization of multiple polarized coils within a single charging pad enhances power transfer efficiency while charging (Figure 3).

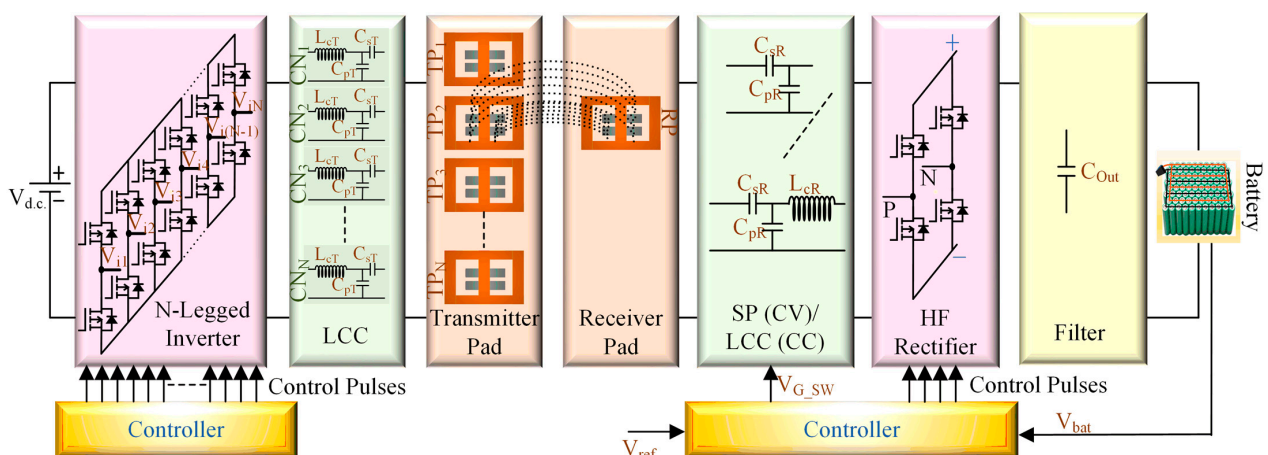


**Figure 3.** Block diagram of proposed quasi-dynamic wireless charging system.

The DD is the optimal transmitter pad, whereas DDQ and BP pads are effective receiver pads in dynamic charging [28]. Due to its single-sided flux channels, susceptibility to aluminum shielding, mean flux path height proportional to half the pad length, and negligible leakage flux from the bottom of the pad, the DD architecture is well-suited for wide-air-gap inductive couplers [29]. These characteristics motivate a preference for a DD pad for a DWC system. Charging pads consist of a high-frequency Litz coil, a ferrite core, and an aluminum shield.

The compensation networks in a wireless charging system enhance performance and optimize the power transfer efficiency [30]. Mono-compensation and multi-compensation are the types of compensation networks based on the resonance characteristics [31]. With a single capacitor,  $C$ , the mono compensation circuits consist of series (S) or parallel (P) units connected to  $C$  such as S–S, S–P, P–S, and P–P. Based on the quantity and configuration of the capacitor ( $c$ ) and the inductor ( $L$ ), the multi-compensation networks are LCC–LCC, LCC–SP, LCL–LCL, S–SP, and LC–LC. A mono-resonant compensation network can be used to operate at a single resonant frequency [32]. The resonance in wireless charging is established by matching the resonant frequency of the transmitter or charging pad with that of the receiver, i.e., the EV being charged [33]. Mono-resonant systems are often preferred for their simplicity in design and ease of implementation. The usage of a fixed resonant frequency facilitates the accurate prediction and control of the system's behavior. However, mono-resonant systems can be susceptible to changes in alignment or environmental conditions, which can result in efficiency losses if the resonance is not maintained [34]. The development of multi-resonant compensation circuits aims to enhance efficiency and adaptability to fluctuating operating conditions. The ability of these circuits to function at various resonant frequencies enhances power transfer efficiency, even in dynamic conditions. Although multi-resonant systems are typically more intricate, they exhibit greater resilience when confronted with alignment variations or environmental circumstances [35].

Modified compensation network topologies were suggested by researchers to attain constant current and voltage (CC and CV) [36,37]. These hybrid topologies ensure the CCCV charging modes with changes in the state of the battery parameters. Constant charging methodologies increase the life span of the batteries [38,39]. The cascaded structure of the LC-network, T-network and  $\pi$ -network ensures constant voltage and current delivery from any type of source [40]. An Additional auxiliary switch (A.SW.) connects and disconnects the resonant elements to modify the network topology and to deliver the load-independent CCCV output. The researchers in [41] proposed the transmitter-side model predictive control method to deliver the CCCV in the DWC system. In the DWC system, LCC–LCC compensation with the phase angle control of the receiver-side active rectifier enhances CC charging [42]. The LCC–LCC network ensures the CC mode, whereas LCC–S ensures the CV mode [43]. The ASW controls mode shifting with respect to the battery parameters [37]. The optimal tuning of the compensation network ensures the soft-switching of the high-frequency high-power (HF-HP) inverter.

The ground-side charging couplers, also known as transmitter pads, are powered by HF-HP inverters. The receiver side rectifier converts the received HF alternating current into constant direct current. The inverter can utilize a variety of switch configurations, such as 4N switches [44], 4 switches [45], or  $2N + 2$  switches [46], to energize the  $N$  transmitter pads. In the high-power transmission, a single pad is excited by a modular inverter [47]. The common-type H-bridge inverter necessitates simple control circuitry only to energize the  $N$ -transmitter pads. However, its effectiveness in DWC systems is limited due to its restricted power range (depending on power semiconductor switches) and the potential for losses resulting from circulating current in uncoupled transmitter pads [48]. The researchers proposed a modular inverter ( $N$ -H bridge inverter) to excite the  $N$ -transmitter pads. Though it has extended power ranges, it is limited due to the requirement of more switches and greater control complexity [49]. The multi-legged inverter [50] is proposed to overcome these limitations, and the inverter excites the multi-transmitter pads. The four transmitter pads were powered by the five-legged inverter used in [51,52]. The receiver-side converter converts HF A.C. into constant D.C. to charge the batteries. Researchers proposed receiver-side control techniques to regulate the power and to perform CCCV charging. The different converters such as active bridge [53], semi-active bridge [54], and D.C.-D.C. converter [55] ensure the achievement of control requirements, thereby making the charging process efficient.

### *Motivation and Contribution*

The DWC's main issues are fluctuations in load, coupling, and output power fluctuation. Through the use of the CCCV charging topology, the system gains load independence. This cutting-edge technology permits real-time adjustments to the charging parameters, adapting the CCCV seamlessly to the vehicles' particular specifications. CCCV charging maximizes energy transfer efficiency by adapting to the battery's condition to facilitate DWC scenarios, irrespective of variations in the vehicles' speed or power demand. By optimizing the charging process to prolong the lifespan of batteries and ensuring secure charging conditions, CCCV charging is renowned for its enhanced battery-friendly charging strategy. It substantially reduces the risk of overcharging or overheating by optimizing the current and voltage throughout the various phases of charging, thereby minimizing cell stress.

Many researchers have proposed a receiver-side control for the minimization of power fluctuations and maintenance of a constant charging profile. The D.C.-D.C. converter is proposed for effective receiver-side power flow control. An additional converter increases the complexity and power conversion stage. The direct current regulator can be eliminated by a receiver-side active bridge rectifier (RS-ABR). The features of an ABR are the elimination of electromagnetic interference, a reduction in voltage losses, the minimization of power factor enhancement, and superior control over the rectification process under changing operating conditions. The merits of the proposed system are mentioned below.

1. Eliminates the need for an additional D.C. regulator on the receiver side to regulate the output power, which reduces the system volume.
2. RS-ABR with a pulse density modulation (PDM) technique regulates the output power and reduces the output ripples compared to a conventional uncontrolled rectifier.
3. A receiver-side hybrid compensation network performs the load-independent CCCV charging process, which increases the reliability of the system.
4. A receiver-side control eliminates the need for battery parameter communication between ground and vehicle assembly to regulate the power flow and shifts the operating mode between CC and CV.
5. A vehicle-side ABR may also be utilized for bi-directional charging with proper control methodology.

This paper suggests using a CCCV charging technique to increase the DWC system's efficiency. To implement the CCCV process, the receiver-side control consists of an ABR with PDM control to manage the power flow to the charging device and a hybrid compensation network. In Sections 2–4, the theoretical analysis, simulation analysis, and experimental analysis of the suggested effective enhanced DWC system are detailed, respectively. Sustainable transportation centered around electric vehicles (EVs) faces several sustainability challenges, including the need for bulky batteries, the inadequate development of charging infrastructure, and the reliance on drivers for the charging process. A proposed solution involves implementing a receiver-side-controlled quasi-dynamic wireless charging system. This system ensures a consistent power supply to the battery, thereby increasing its lifespan and reducing the need for frequent replacements, contributing to sustainability efforts. Additionally, integrating a receiver-side PDM-based active bridge rectifier helps regulate output power, eliminating the need for an additional DC regulator, thereby reducing system volume and resource consumption. Overall, this quasi-dynamic wireless charging system addresses sustainability concerns by reducing battery size, extending EV driving range, and enhancing adaptability through its drive-and-charge approach and optimized ferrite core structure. These improvements result in reduced power requirements, lower carbon emissions, and a more sustainable transportation ecosystem. Furthermore, on-road charging infrastructure eliminates the need for extensive land use for station deployment, conserving natural resources, reducing environmental impact, and simultaneously reducing waiting times for EV charging, thereby encouraging the wider adoption of sustainable transportation practices.

## 2. Proposed System Components: A Theoretical Analysis

The proposed charging system enhances the receiver-side power control and implements CCCV charging to deliver constant voltage and current to the charging system. An advantageous feature of the DWC system is that the five-legged SiC inverter excites the four DD-shaped charging transmitters and the LCC resonant circuit by circulating a constant current. The FPGA controller generates driving pulses to control the five-legged inverter concerning the receiver pad position. An ABR controls the power delivered to the storage device, a hybrid resonant network (LCC in CC and SP in CV mode), and an identical DD-shaped receiving pad make up the receiver-side components. Pulses generated by PDM regulate the ABR's low-frequency pulse width, which in response controls the output power. The A.S.W. connects and disconnects the receiver-side series compensation inductor to shift the mode from CC to CV, respectively. The charging system delivers CC in LCC–LCC configuration and CV in LCC–SP configuration.

### 2.1. Charging Couplers

The proposed charging system utilizes symmetrical DD-shaped charging couplers to transfer the power. The charging coupler has better horizontal misalignment tolerance and generates vertical flux in half of the pad dimension [56]. The dimensions of the charging coupler, the vertical distance between charging pads, and the adjacent spacing between the transmitter pads are illustrated in Figure 4. The 700 mm × 350 mm sized DD pad is developed with 38 AWG Litz wire. The optimal gap is allowed between the transmitter pads (575 mm) to reduce the cross-coupling effect. The 360 mm length ferrite structure enhances the flux distribution and increases the inductance of the charging pad. The 2 mm aluminum shielding reduces the electromagnetic emissions around the transmitter pads. It is hard to determine the inductance parameters of the DD pad with mathematical expressions. The Ansys FEA tool assists in achieving the inductance parameters concerning the power transferring level and vertical gap.

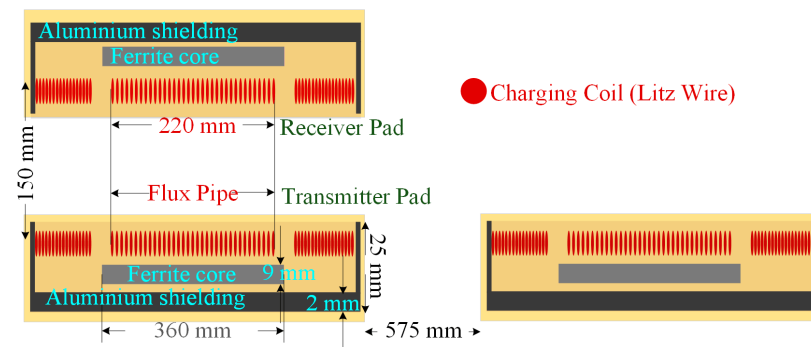


Figure 4. Geometry representation of quasi-dynamic charging coupler.

### 2.2. Five-Legged Inverter

The charging system utilizes a five-legged inverter to excite the four DD-shaped transmitter pads. The researchers suggested a multi-legged inverter [57,58] to overcome the demerits of the common H-bridge. The multi-legged inverter excites the multi-transmitter pads concerning the receiver position which is favorable in the DWC system. The constant D.C. voltage,  $V_{D.C.}$  is fed to the HFHPI, and the inverter is driven by the FPGA controller.

$$V_i = \frac{4V_{d.c.}}{\pi\sqrt{2}} \cos \theta \quad (1)$$

$$I_i = \frac{4I_{d.c.}}{\pi\sqrt{2}} \cos \theta \quad (2)$$

The minimum dead time is allowed by the phase angle,  $\theta$ , to enhance soft switching. The power transfer characteristics are affected by the  $\theta$  with a permissible value parallel

to its minimum angle. Leg 1 and 2 energize the transmitter pad 1, whereas Leg 2 and 3 energize the transmitter pad 2. The fundamental rms output voltage of an inverter,  $V_i$ , and current,  $I_i$ , from the Fourier series are given by (1) and (2). By adjusting  $\theta$ ,  $V_i$  and  $I_i$  can be varied from  $(4V_{D.C.}/\sqrt{(2\pi)})$  to 0 and  $(4I_{D.C.}/\sqrt{(2\pi)})$  to 0 at constant resonant frequency,  $f_r$ , and constant input D.C. [59,60]. The  $V_{D.C.}$  and  $I_{D.C.}$  represent inverter D.C. input voltage and current. As per SAE J2954, the controller drives the five-legged inverter with 85 kHz driving pulses (Figure 5).

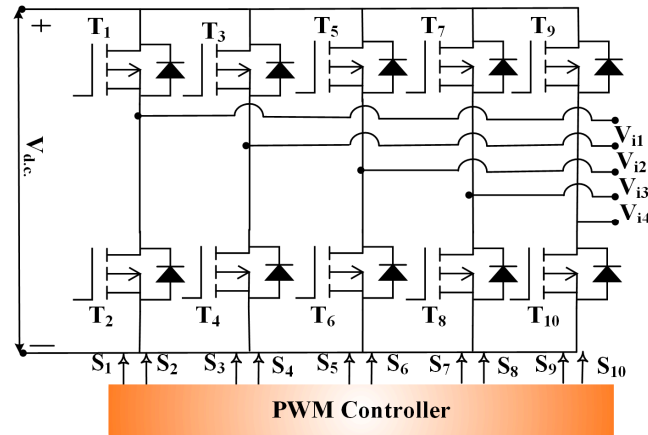


**Figure 5.** Five-legged inverter topology.

### 2.3. Compensation Network

The compensation network enhances the power transfer efficiency and compensates the VAR. The transmitter side utilizes an LCC network that circulates the constant current through the transmitter pad, which is preferable in a DWC system. The receiver side utilizes hybrid compensation that includes LCC and SP to perform CCCV charging. The LCC–LCC network ensures CC mode and the LCC–SP network ensures CV mode to perform the charging operations.

#### 2.3.1. Load-Independent CC Mode Analysis with D–LCC Network

The individual or combinational cascaded structure of LC-network,  $\pi$ -network, and T-network ensures the constant charging of the charging system. Figure 6 represents the double-sided LCC resonant networks' A.C. equivalent. The network is arranged in a cascaded structure, and the network parameters are designed with respect to the cascaded structure arrangements to deliver the constant current. The figure addresses the type of network and its conversion of sources. The second-order LC network converts the constant voltage source into a current source and the cascaded series LC network,  $\pi$  network, and series inductor ensure the constant current delivery to the charging device independent of load variations. The transmitter-side resonant network elements are a series compensation capacitor and inductor ( $C_{sT}$  and  $L_{cR}$ ) and a parallel capacitor ( $C_{pT}$ ), and the receiver-side resonant network elements are a series compensation capacitor and inductor ( $C_{sR}$  and  $L_{cR}$ ) and a parallel capacitor ( $C_{pT}$ ). The transmitter and receiver pad inductances are  $L_T$  and  $L_R$ . The mutual inductance between the transmitter and receiver pad,  $L_M$ , depends on the coupling coefficient,  $k$ . The A.C. equivalent voltage,  $V_b$ , and the current,  $I_b$ , depend on the A.C. equivalent resistance,  $R_{A.C.}$ . When the receiver-side elements are transferred to the transmitter side, the transformation ratio factor,  $n$  ( $=L_R/L_T$ ), must be considered. Equations (3)–(5) provide the relationship to achieve load-independent constant charging.

$$j\omega_{cc}L_{cT} + \frac{1}{j\omega_{cc}C_{pT}} = 0 \quad (3)$$

$$j\omega_{cc}L_T + \frac{1}{j\omega_{cc}C_{sT}} = 0 \quad (4)$$

$$j\omega_{cc} \left( \frac{L_R}{n^2} \right) + \frac{1}{j\omega_{cc}(C_{sR}n^2)} + \frac{1}{j\omega_{cc}(C_{pR}n^2)} = 0 \quad (5)$$

$$I_{bcc} = -jn^2V_i\omega_{cc}^3L_M C_{pT}C_{pR} \quad (6)$$

$$G_{Tcc} = \left| \frac{I_{bcc}}{V_i} \right| = n^2\omega_{cc}^3L_M C_{pT}C_{pR} \quad (7)$$

$$\left( \frac{C_{pT} + C_{sT}}{\omega_{cc}C_{pT}C_{sT}} \right) - \omega_{cc}L_T + \omega_{cc}^3n^2C_{pR}L_M^2 \left( 1 - \left( \omega_{cc}^2L_{cR}C_{pR} \right) \right) = 0 \quad (8)$$

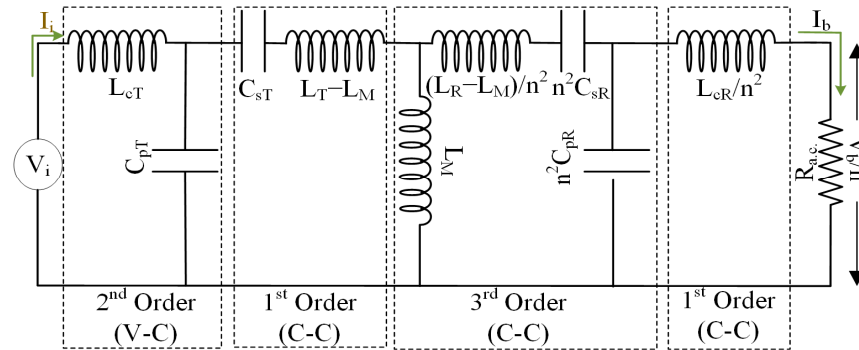


**Figure 6.** a.c. equivalent circuit of a double-sided LCC network.

The CC delivered to an  $R_{A-C}$  in a CC mode,  $I_{bcc}$ , can be determined using (6), and the transconductance of an equivalent network,  $G_{TCC}$ , can be achieved using (7). At constant  $f_r$ ,  $C_{pT}$ , and  $C_{pR}$ ,  $I_{bcc}$  is proportional to  $L_M$  and  $V_{i,rms}$ .  $\omega_{cc}$  refers to the angular resonant frequency in the CC mode. The dual-side LCC network ensures CC circulation, which is a desirable factor of the DWC system [61,62]. The relationship to attain the zero-phase angle in the CC mode is denoted by (8). Achieving soft switching in an inverter needs a modest inductive nature of the CC mode network's total input impedance,  $Z_{inCC}$ . The imaginary part of the  $Z_{inCC}$  is zero under the resonant condition. With an increase in  $R_{A-C}$ ,  $V_b$  increases and the network maintains constant  $I_b$ . The LCC network parameters can be achieved as outlined in [63–65].

### 2.3.2. Load-Independent CC Mode Analysis with LCC–SP Circuit

The LCC–SP network delivers the load-independent constant voltage to the charging device and assists in implementing CV mode charging. The cascaded T network assures load-independent constant voltage delivery with constant input voltage and minimizes the input apparent power in the charging system. Usually, a third-order T network converts a constant voltage source into a voltage source. So, the two series connected third-order network delivers the constant voltage to the charging device independent of load variations. Equations (9)–(12) denote the relationship to achieve CV mode charging with an LCC–SP network (Figure 7).  $C_{pT}$  stabilizes  $V_b$  concerning the variations in  $R_{A-C}$ .  $\omega_{cv}$  refers to the angular resonant frequency in CV mode.

$$j\omega_{cv}L_{TK_{cv}} + \frac{1}{j\omega_{cv}C_{sTK_{cv}}} = \frac{1}{j\omega_r C_{sT}} + j\omega_r(L_T - L_M) \quad (9)$$

$$\frac{1}{j\omega_{cv}C_{sRK_{cv}}} = \frac{1}{j\omega_r n^2 C_{sR}} + j\omega_r \frac{(L_R - L_M)}{n^2} \quad (10)$$

$$\omega_{cv} = \sqrt{\left( \frac{1}{L_{cT}C_{pT}} \right) + \left( \frac{1}{L_{TK_{cv}}C_{pT}} \right)} \quad (11)$$

$$\omega_{cv} = \frac{1}{\sqrt{(L_M C_{sTk_{cv}}) + (L_M C_{sRk_{cv}}^2)}} \tag{12}$$

The CV mode voltage gain of the charging system is given by (13).

$$\text{CV Mode Voltage Gain, } G_{T_{cv}} = \left( \frac{L_{Tk_{cv}}}{L_{cT}} \right) \left( \frac{C_{sTk_{cv}}}{C_{sRk_{cv}}^2} \right) \tag{13}$$

The voltage gain of the charging system during CV mode is more significant than the current gain. The higher voltage gain improves the system efficiency. The ASW disconnects the  $L_{cR}$  from the network when the battery voltage,  $V_{bat}$ , reaches the preset value.

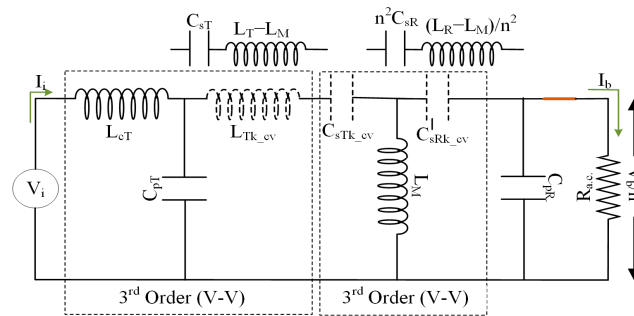


Figure 7. LCC-SP network’s a.c. equivalent circuit.

#### 2.4. Receiver-Side Active Bridge Rectifier

Usually, the charging system utilizes separate D.C. regulators to enhance power delivery. In this article, the receiver-side ABR regulates the output power with a PDM driving pulse. The PDM driving pulses regulate the output power through pulse density variations in the controller pulses,  $d$ , without adjusting the  $f_r$ . The A.C. equivalent voltage is directly proportional to the density of the PDM pulse that is mentioned in (14).

$$V_b = \frac{2\sqrt{2}}{\pi} V_{bat} d \cos \theta_1 \tag{14}$$

$$R_{a.c.} = \frac{8}{\pi^2} d^2 R_{bat} \tag{15}$$

$$P_{0-PDM} = P_{rated} \times d^2 \tag{16}$$

where the battery’s equivalent resistance, voltage, and current are  $R_{bat}$ ,  $V_{bat}$ , and  $I_{bat}$ , respectively, and  $d$  is the ratio of the ON period of the PDM pulses,  $T_{ON, PDM}$ , to the total period of PDM control pulses,  $T_{PDM}$ . Consequently,  $d$  and  $\theta$  decide the charging system power,  $P_{out}$ . Equation (16) represents the relationship of PDM output power,  $P_{PDM}$ , and rated output power,  $P_{rated}$ , with  $d$ . See Figure 8.

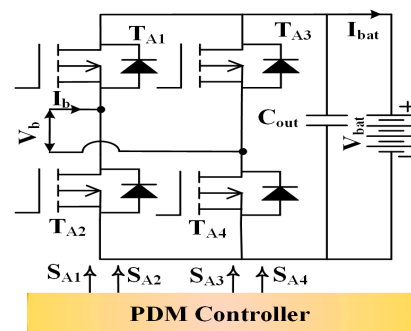


Figure 8. PDM-controlled active bridge rectifier.

### 3. Proposed Charging System Components: Simulation Analysis

#### 3.1. Charging Couplers

Through the optimal design of charging pads, power transfer efficiency is maximized and misalignment tolerance is enhanced. The Ansys Electronic Desktop assists in developing the DD-shaped optimal charging coupler. The charging coupler must be wound tightly to achieve effective inductive parameters. By minimizing the distance between turns and increasing the number of turns, the inductance of the coil increases. The optimal flux pipe (center portion of the charging coil) improves the flux density. The optimal adjacent gap between the transmitter pads reduces the cross-coupling effect.

The addition of a ferrite core to the charging coupler increases the inductance and improves the flux density distribution. Without increasing the number of ferrites and optimal placement of ferrite bars, the core structure has to be added. The addition of aluminum shielding also increases the inductances. Increasing the shielding thickness and placing the shielding close to the ferrite bars increases the pad's inductance. So, the optimal charging pad can be developed by considering the above-mentioned parameters. The charging coupler is simulated in the Ansys Eddy current solver with a 38 AWG, 1050 strand conductor, and a 10 A current is allowed to excite the transmitter pad. The vertical distance between the charging pads is 150 mm. Figure 4 illustrates the charging coupler dimensions, and Figure 9 represents the magnetic flux density spectrum concerning the various misalignment conditions.

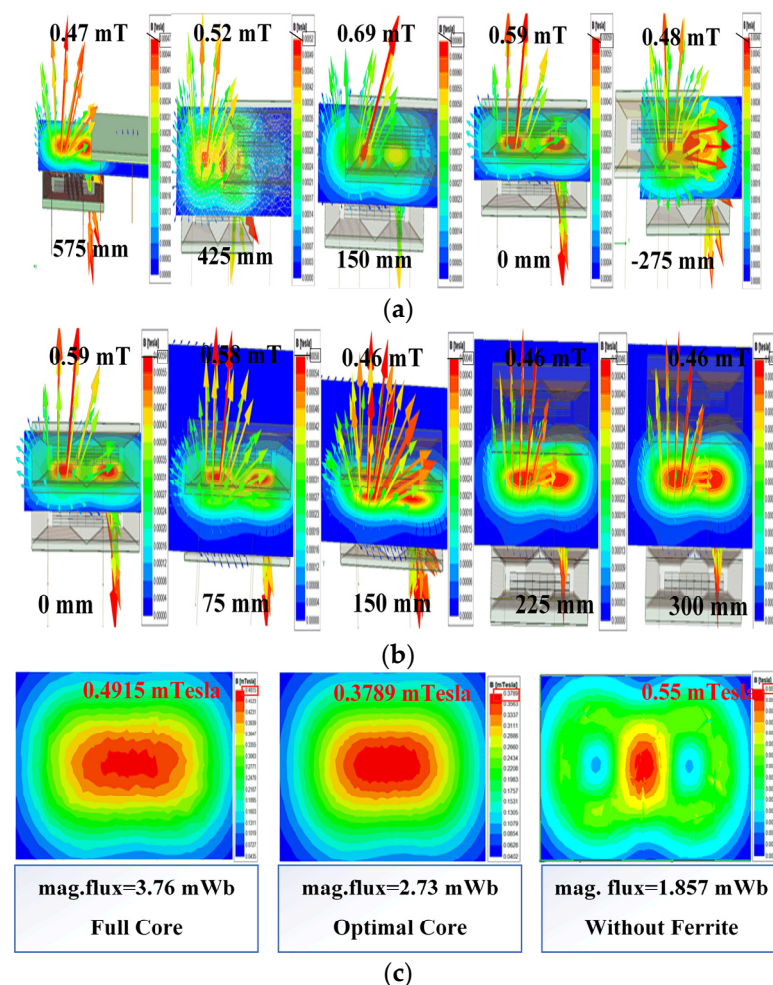


**Figure 9.** FEA analysis of the charging coupler. (a) Longitudinal misalignment. (b) Lateral misalignment. (c) Magnetic field distribution for different Ferrite structure.

### 3.2. Five-Legged Inverter

The transmitter-side inverter excites the transmitter pads with respect to the receiver pad position. The ideal period is allowed during the leg transition to achieve a smooth transition. The phase shift modulation PWM pulses drive the switches of the Five-legged inverter (Figure 10). Leg 1 and 2 excite the transmitter pad 1, whereas Leg 2 and 3 excite the transmitter pad 2. The excitation sequence continues, and the leg transition occurs with respect to the receiver pad position. Driving pulses are produced by the controller at 85 kHz following SAE J2954. The transmitter-side FPGA controller is programmed with pre-defined switching sequence variations. These variations ensure that legs 1 and 2 of the five-legged inverter operate for a particular period and then leg 1 automatically disconnects and legs 2 and 3 operate. The receiver pad has to move over the transmitter pad with this pre-defined sequence variation in our proposed charging system to maximize the power transfer efficiency. The inverter's quasi-square wave A.C. output is fed to the equivalent circuit, and it resonates at an 85 kHz frequency. By adjusting the  $\theta$ , it is feasible to regulate the inverter's output current and voltage. Equations (1) and (2) provide the relationship between inverter output and phase shift angle. The increases in  $\theta$  reduce the output of the inverter concerning the cosine factor. A minimum  $\theta$  between the driving pulses of  $T_1$  and  $T_4$  improves the soft-switching ability of an inverter. Figure 11b represents the inverter's parameters concerning the variations in  $\theta$ . The inverter must be operated slightly higher than the resonant frequency to achieve soft switching. While increasing the resonant frequency by a factor of 0.01, the magnitude of the output current, voltage, and power are increased. When increasing  $\theta$ , the output current and voltage of an inverter decrease from the rated value. The output current and voltage of an inverter are directly proportional to the cosine of the phase shift angle. So, while increasing  $\theta$ , the voltage and current of an inverter decrease, and the corresponding output power also decreases. The characteristic curves are obtained by adjusting the  $\theta$ , and the corresponding variations are noted in the Simulink setup of the charging system. The curves are achieved by varying the shift angles from  $0^\circ$  to  $75^\circ$ , and the corresponding values are recorded.

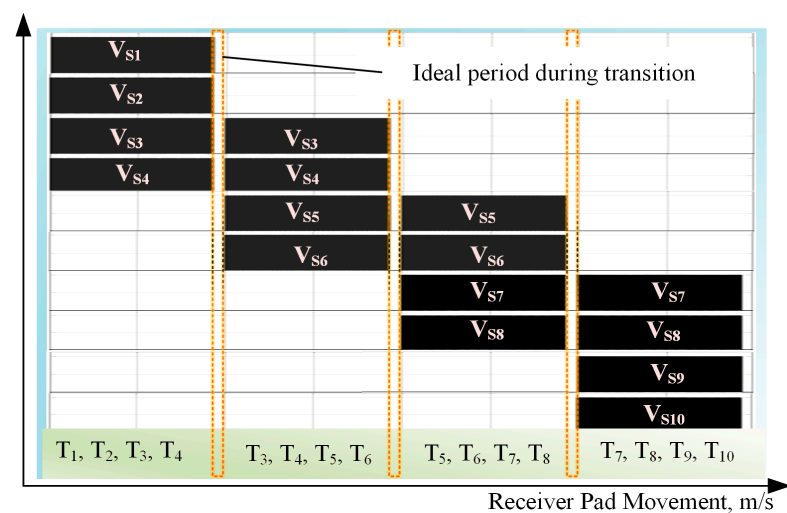
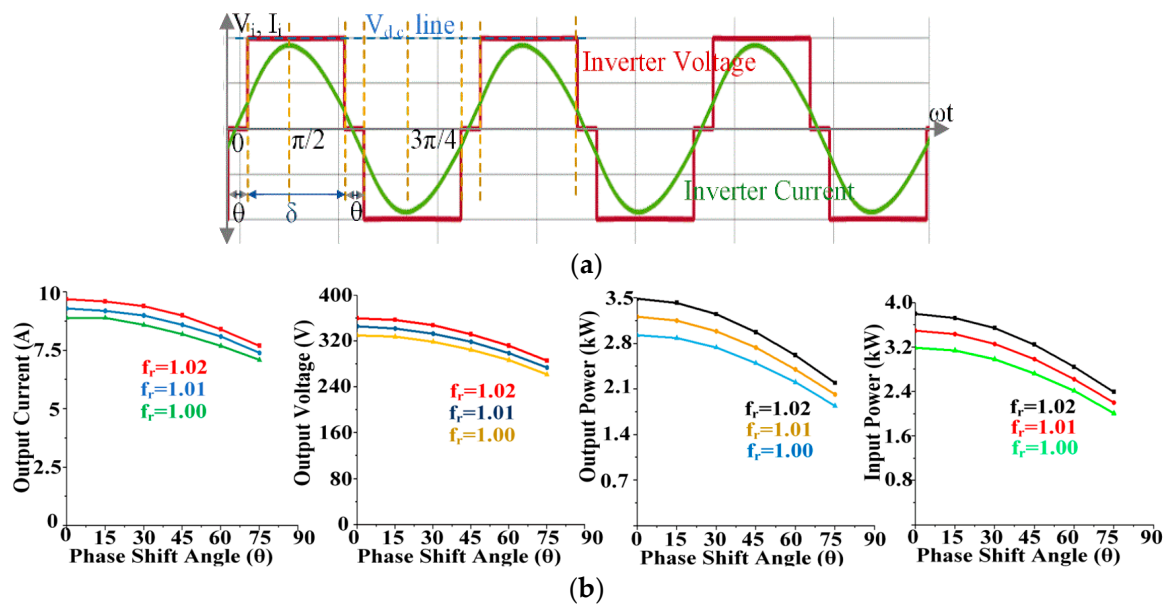


Figure 10. Five-legged inverter's control pulse pattern.



**Figure 11.** The simulated output waveform of an inverter. (a) Voltage and current of two-legged inverter. (b) Variation in inverter output concerning the phase shift angle.

### 3.3. Hybrid Compensation Network

The LCC–LCC network delivers the constant current, whereas the LCC–SP network delivers the constant voltage to the charging system. In a resonant network,  $L_{cR}$  stabilizes the  $I_b$ , and  $C_{pR}$  stabilizes the  $V_b$ . Figure 12 illustrates the simulation curves of the LCC–LCC and LCC–SP network at rated  $L_m$ . When  $L_m$  decreases, the output voltage and current magnitude decrease. A minimum phase shift angle is introduced between the conduction pair switches to perform the soft switching. The 3.3 kW wireless charging system is developed with the receiver-side switchable compensated system (LCC–LCC/SP) in MATLAB Simulink, and the figures show the compensated structures characteristics curves.

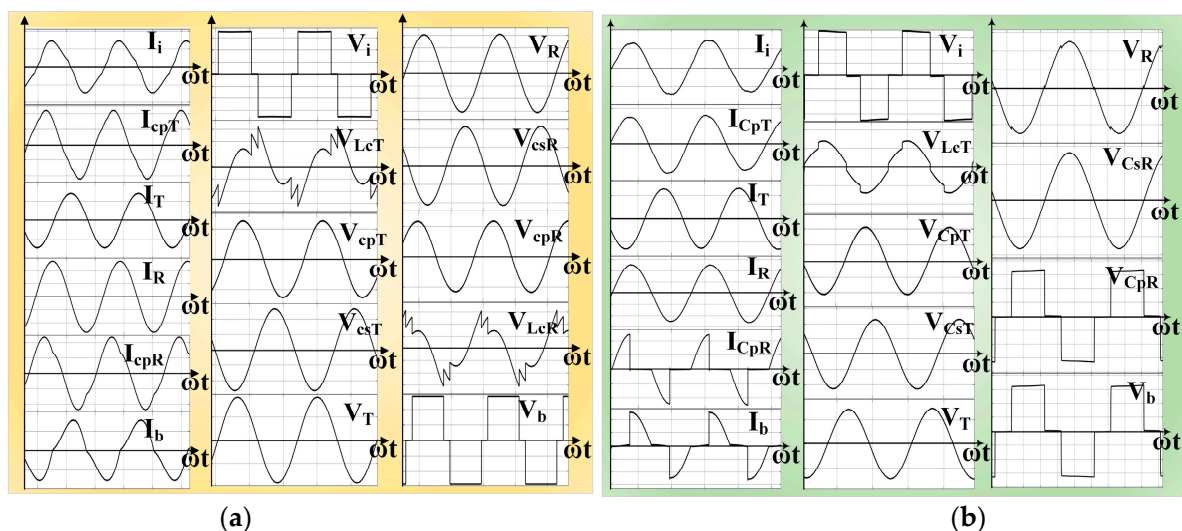


**Figure 12.** Simulated output waveform. (a) Double-sided LCC network. (b) LCC–SP network.

Figure 13 illustrates the load-independent frequency sweep characteristics curve of the proposed charging system. Figure 13a represents the voltage gain characteristics and Figure 13b represents the current gain characteristics of the LCC–SP and LCC–LCC networks, respectively. The LCC–SP network delivers the constant voltage independent

of the load variations. The voltage gain curves of the LCC-SP network concerning the frequency sweep are achieved for 100%, 120%, 140%, and 160% of load variations. The gain value reaches the maximum at three different frequencies due to bifurcation. The charging system has unique voltage gain when the LCC-SP network operates at the CV mode resonant frequency,  $\omega_{cv}$ . The LCC-LCC network delivers a constant current independent of the load variations. The current gain curves of the LCC-LCC network concerning the frequency sweep are achieved for 100%, 80%, 60%, and 40% load variations. The current gain reaches two maximum levels due to bifurcation. The network has a unique current gain when operating at the CC mode resonant frequency,  $\omega_{cc}$ . Here, the 100% load conditions refer to the rated equivalent resistance of the battery, and the magnitude at the rated operating condition is  $37.2 \Omega$ . The charging system has a unique resonant frequency, and it operates at 85 kHz in both modes.

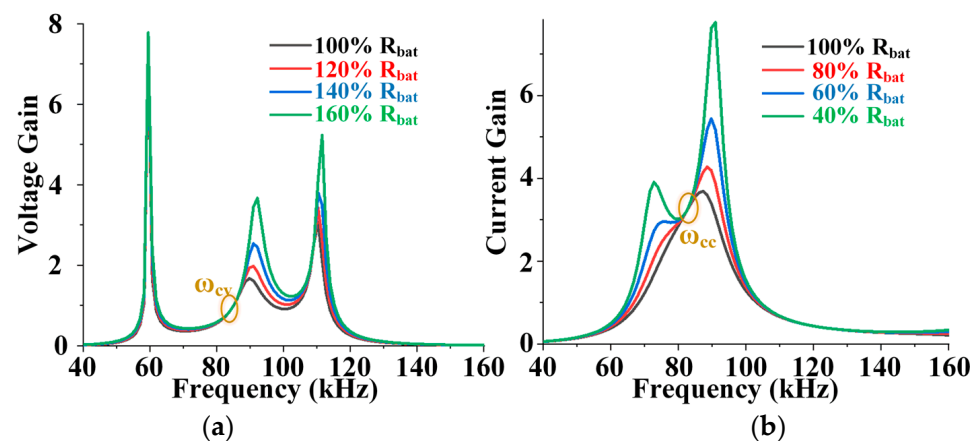


**Figure 13.** Frequency sweep curves. (a) LCC-SP network. (b) LCC-LCC network.

### 3.4. Receiver-Side Active Bridge Rectifier

The receiver-side ABR assists in regulating the power delivered to the charging device whenever the charging system requires power lesser than the rated value. An auxiliary switch connected across the  $L_{cr}$  configures the receiver-side resonant network. When the switch is closed, an LCC-SP configuration delivers the constant voltage. When the switch is opened, an LCC-LCC configuration delivers the constant current. An ABR regulates the power delivered to the charging device by adjusting  $d$ . Figures 14 and 15 illustrate the D-LCC compensated system's response curve, whereas Figures 16 and 17 illustrate the LCC-SP compensated system's response curve. In these figures, the density of the PDM pulses varied by 80% and 60%. Figure 18 depicts the characteristic waveforms of the charging system while the receiver-side compensated network mode shifts from SP to LCC. The output of the charging system depends on the density of the pulses, and the relationship between the pulse density and the output voltage and power is represented in Equations (14) and (16). The density of the pulses is directly proportional to the A.C. equivalent voltage. The power and voltage delivered to the charging system can be varied with respect to the variations in  $d$ , which is represented in (14) and (16). The 80% and 60% of PDM terms mean that the frequency of the PDM signal (low-frequency signal compared with 85 kHz signal to achieve PDM) was reduced by factors of 0.8 and 0.6, respectively, and the ideal period (non-active period) of the output waveform is increased. The output power can be regulated by adjusting the  $d$  factor, and the square of the  $d$  is directly proportional to the output power.

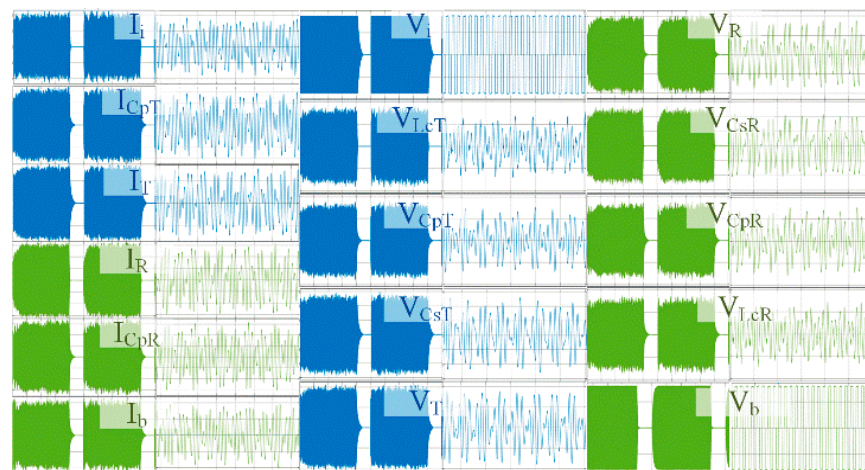


Figure 14. Simulation curves of double-sided LCC network with 80% PDM.

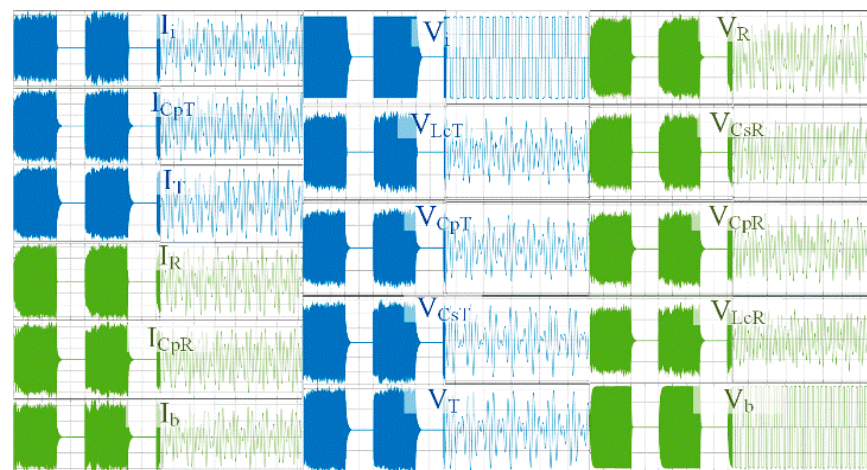


Figure 15. Simulation curves of double-sided LCC network with 60% PDM.

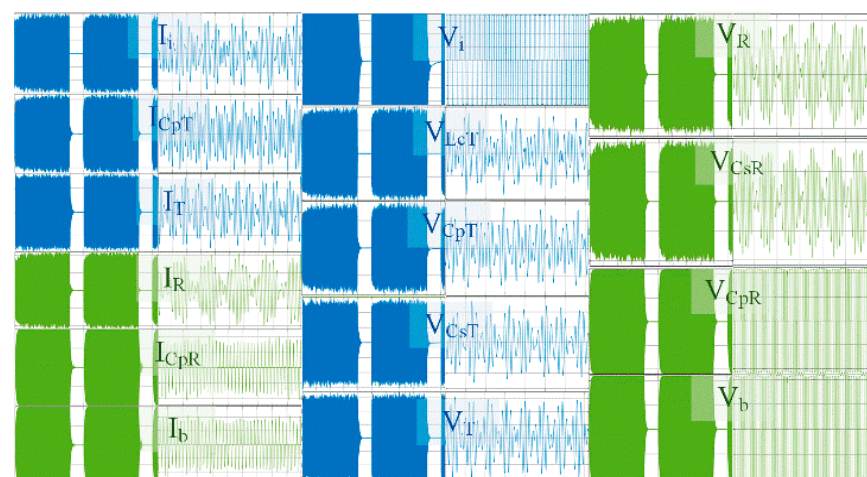


Figure 16. Simulation curves of LCC-SP network with 80% PDM.

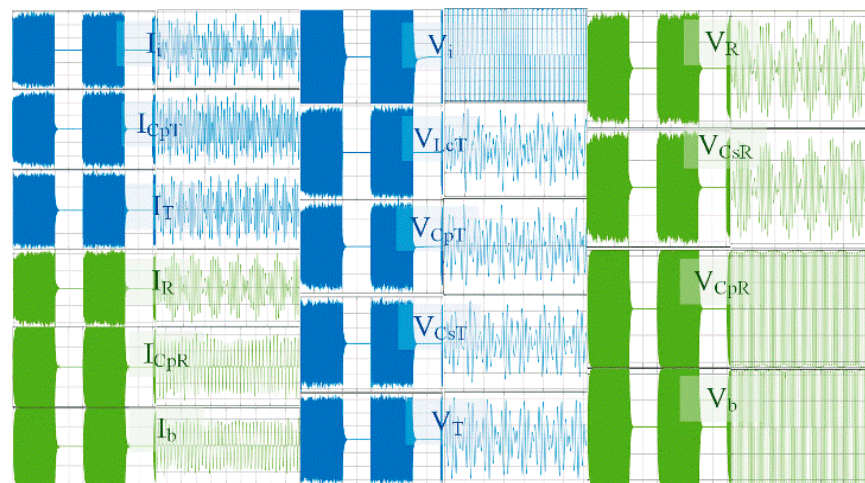


Figure 17. Simulation curves of LCC-SP network with 60% PDM.

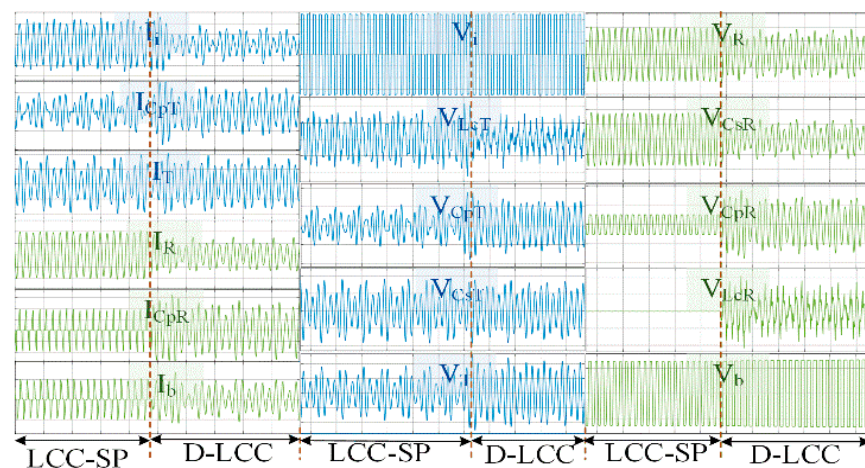


Figure 18. Simulation curves of LCC-SP mode to LCC-LCC (D-LCC) mode-shifting instant.

#### 4. Experimental Analysis

A 3.3 kW five-legged inverter-fed hybrid network compensated receiver-side power-regulated charging system is developed to demonstrate the proposed charging topology. An LCC-LCC network delivers the constant current, whereas an LCC-SP network delivers the constant voltage. The auxiliary switch connects and disconnects the  $L_{cR}$  to modify the receiver-side resonant network.

PDM pulses drive the receiver-side ABR, which regulates output power.  $P_{out}$  can be adjusted following (16) by varying  $d$ . The five-legged inverter excites the transmitters based on the position of the receiver. The receiver pad moves down the track as the control pulses of the inverter shift the legs. Legs 1 and 2 energize  $TP_1$ , while Legs 2 and 3 energize  $TP_2$ . To minimize the impact of transients, the least dead time is permitted while shifting the inverter legs. Experimental analysis curves of the proposed charging system are represented in Figures 19–23. Figures 19 and 20 represent the PDM-regulated ABR-controlled LCC-LCC and LCC-SP compensated charging system. The density of the pulses is adjusted to 80%, and the corresponding characteristics curves across the various elements of the system are observed. The average power,  $P_{avg}$ , delivered to the system is varied with respect to the relationship between  $P_{avg}$ ,  $P_{rated}$ , and  $d$ , which is described in (16). The receiver-side hybrid resonant network ensures the delivery of constant voltage and current concerning the status of the charging device. If the charging device voltage,  $V_{bat}$ , is lower than the reference voltage,  $V_{ref}$ , the auxiliary switch opens, and the LCC network delivers the constant current independent of load variations. Once  $V_{bat}$  exceeds  $V_{ref}$ , the

switch closes, and  $L_{cR}$  short circuits. The SP network delivers the constant voltage to the charging device. Figure 23 represents the charging systems' constant current and voltage delivery independent of the load variations. Figures 21 and 22 represent the experimental waveforms of the charging system during operating mode transition. The maximum charging system efficiency is 93.4%.

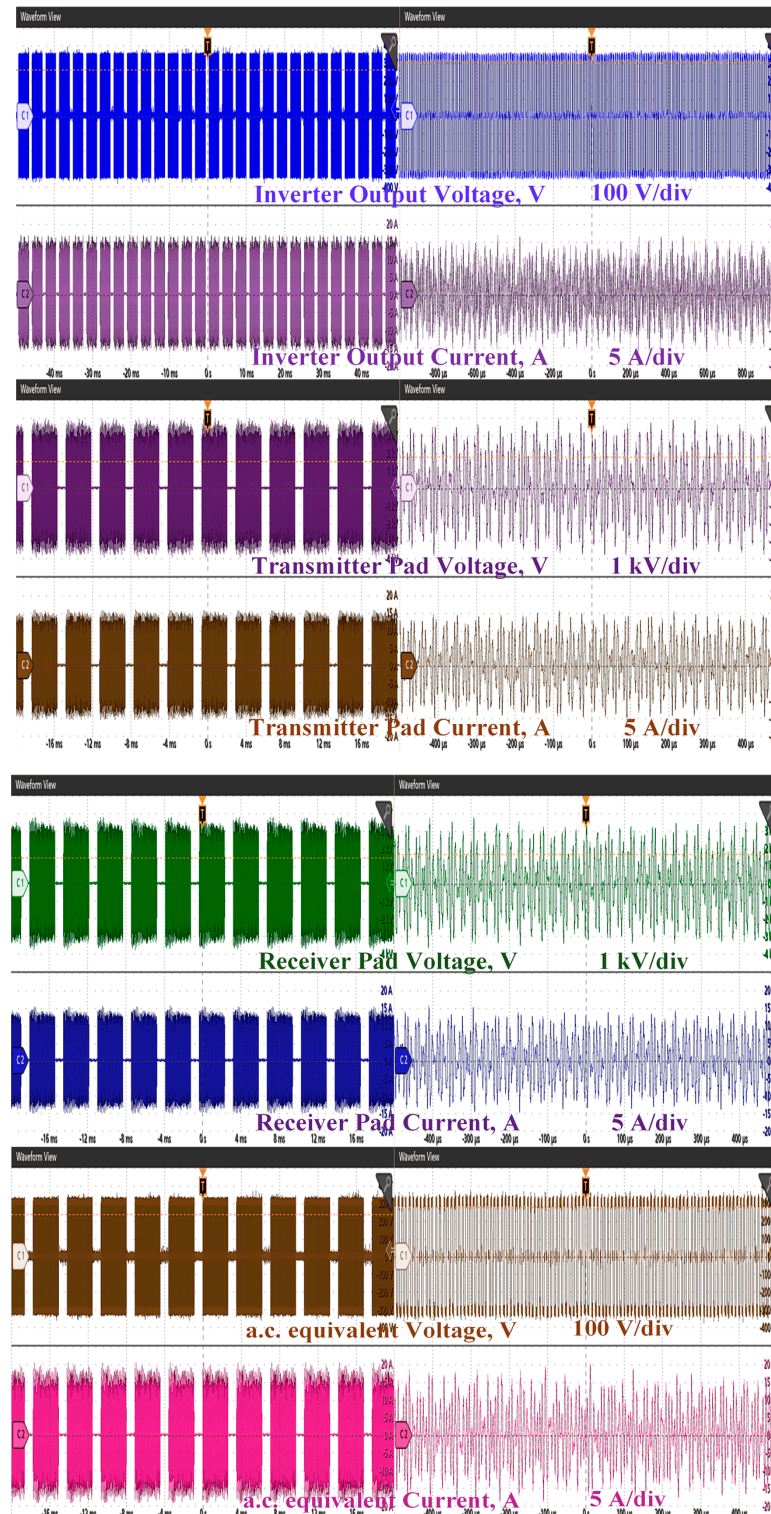


Figure 19. Experimental curves of LCC-LCC compensated system at 80% PDM.

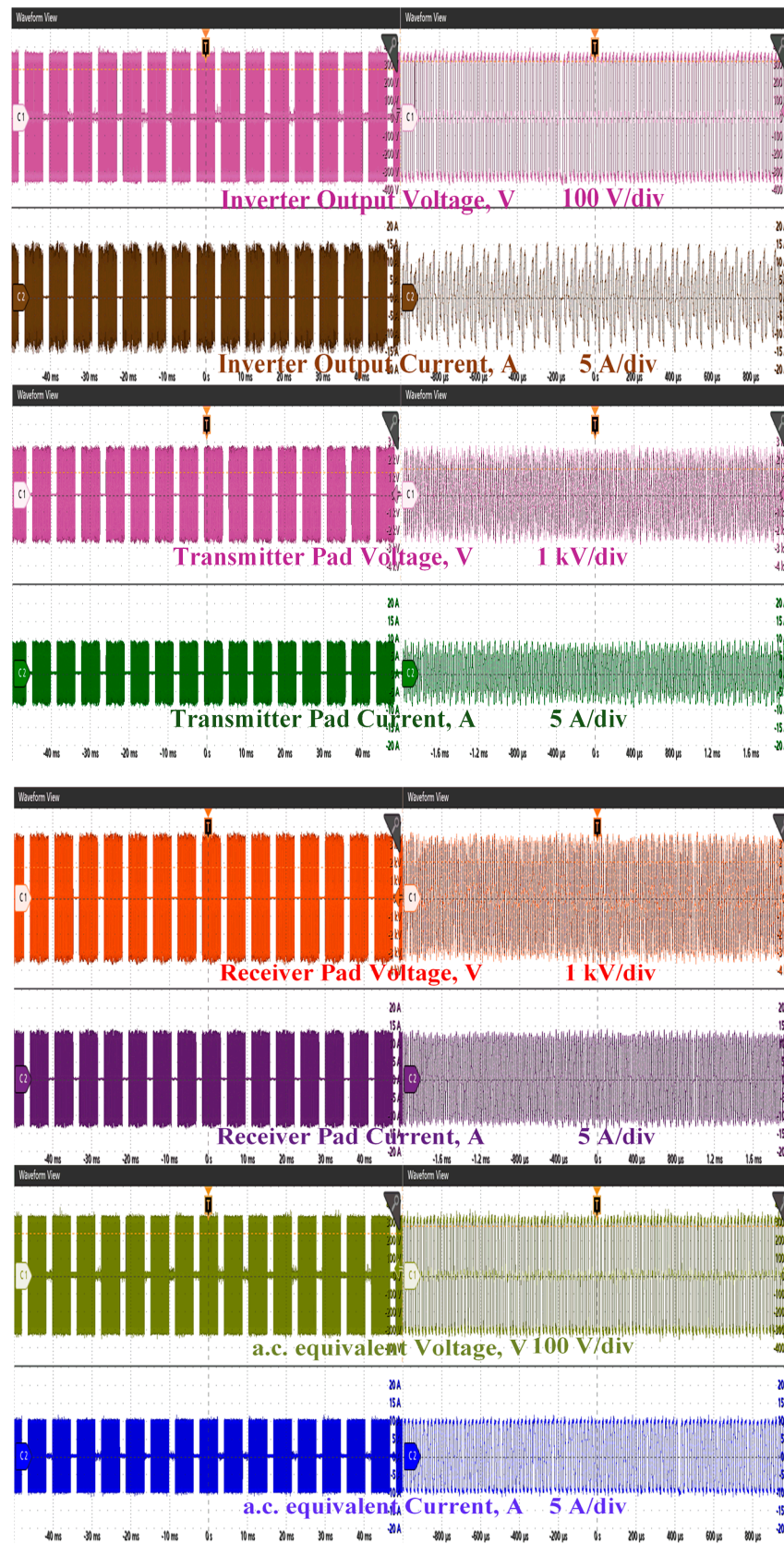


Figure 20. Experimental curves of LCC-SP compensated system at 80% PDM.

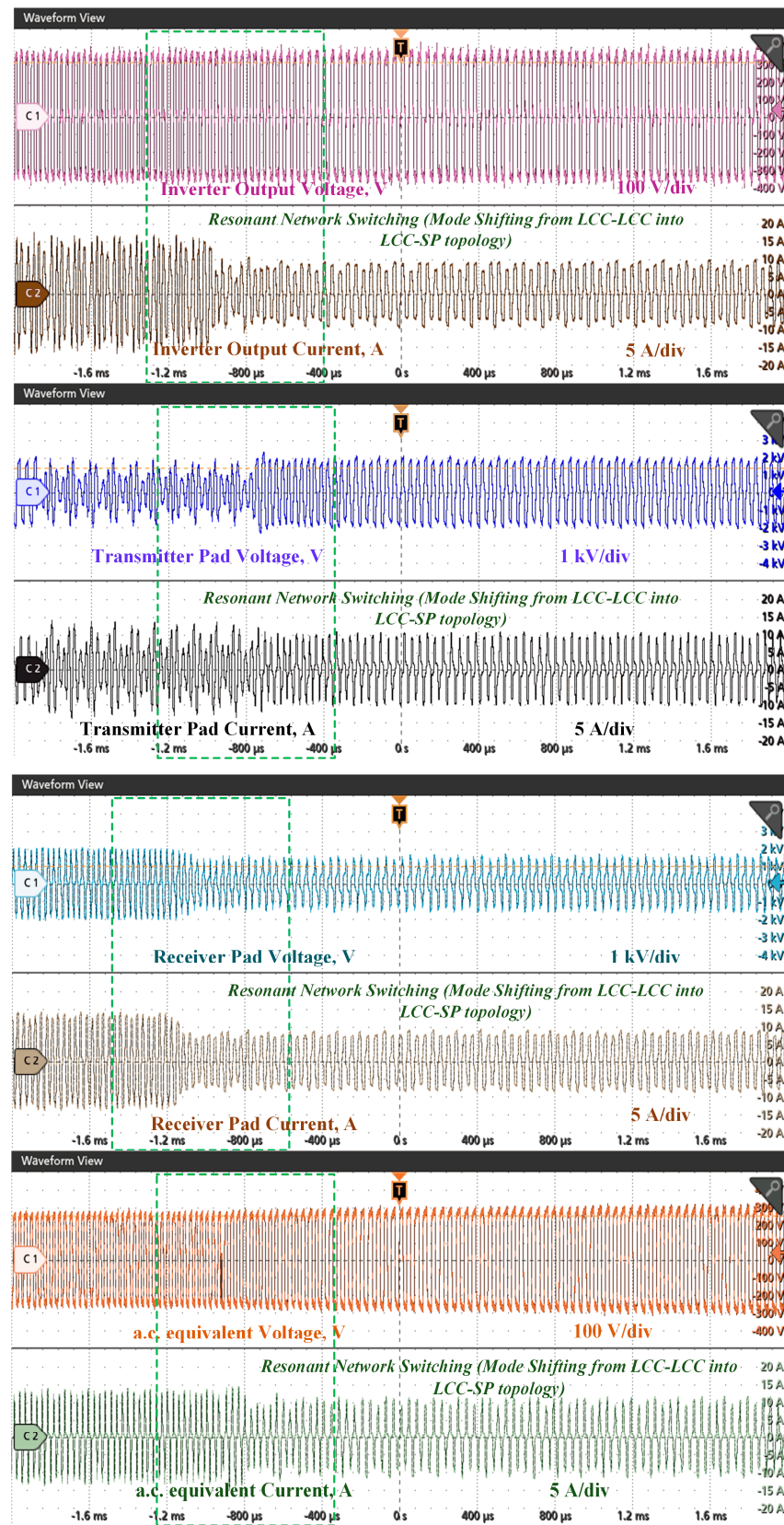
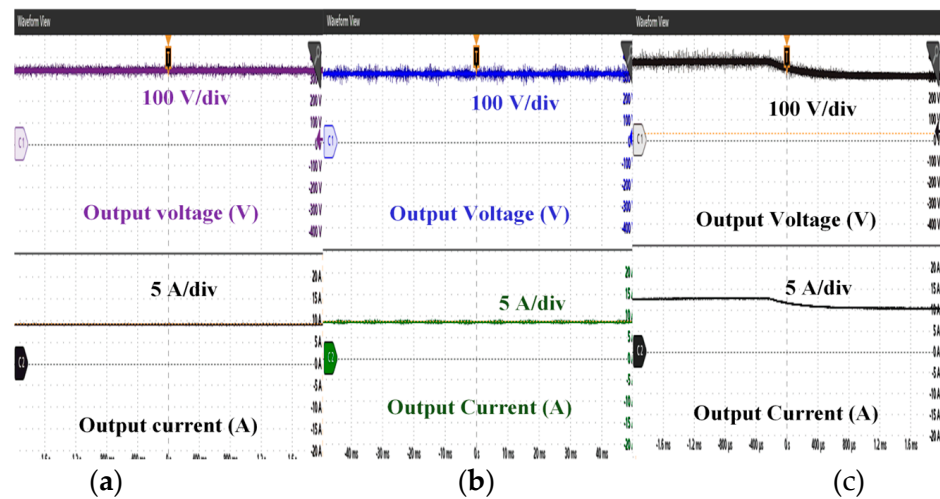
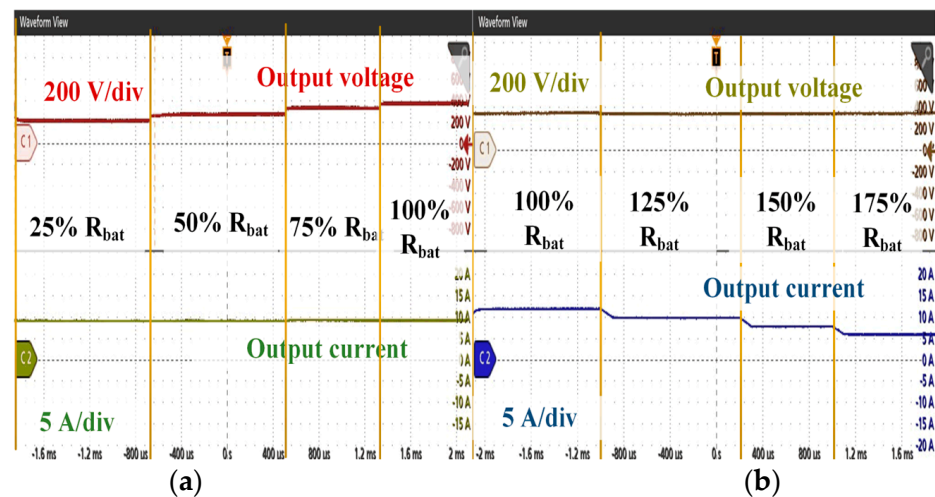


Figure 21. Experimental curves of a proposed charging system during mode switching (D-LCC to LCC-SP).



**Figure 22.** Experimental output curves of a proposed charging system. (a) LCC–LCC. (b) LCC–SP. (c) Switching from LCC–LCC to LCC–SP.



**Figure 23.** Experimental output curves of a proposed charging system. (a) LCC–LCC (load-independent constant current). (b) LCC–SP (load-independent constant voltage).

An experimental setup of the developed charging system is represented in Figure 24. The power is transferred by a 700 mm × 350 mm DD pad, and the charging pad has a 38 SWG Litz wire, a 9 mm thick ferrite core, and 2 mm of aluminum shielding. The charging coupler is excited by a 3.3 kW, 350 V, SiC-integrated five-legged inverter. The transmitter-side LCC network circulates the constant current in a transmitter pad, which is beneficial to the dynamic wireless charging system. The ferrite-cored inductor ensures the constant current in the charging coupler. The receiver-side hybrid compensation LCC–SP topology ensures constant charging. The SiC-integrated receiver-side bridge rectifier regulates the power delivered to the charging device by varying the density of the pulses. The FPGA controller delivers the controlling pulses to the transmitter- and receiver-side converter, and the system can perform constant charging and output power regulation. Table 1 illustrates the existing receiver-side controlled charging topology and parameters of the proposed topology.

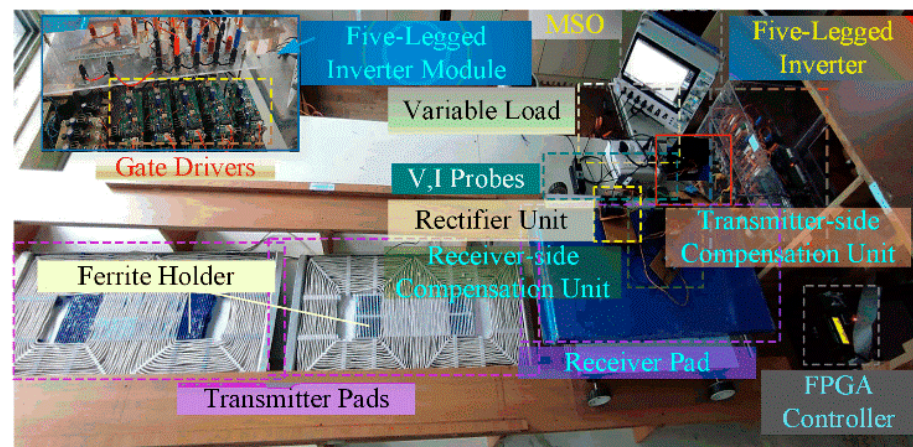


Figure 24. Experimental setup of the proposed charging system.

Table 1. Different charging parameter regulating topologies.

Ref.	Control Side	Control Method	Regulating Parameters	kW	Airgap (mm)	f (kHz)	Efficiency (% $\eta$ )	WPT Method
[66]	Dual-side active converter	Triple-phase shift control	Efficiency and output voltage	1.5	-	85	83.4–93.6	Stationary
[67]	Dual-side active converter	Fuzzy-based PDM	Power transfer efficiency	3.7	150	85	93	Stationary
[68]	Receiver-side three-level buck	Composite control	Switching stress reduction and output power regulation	2.6	-	20	87.2	Dynamic
[69]	Receiver-side buck converter	Model predictive control	Output power	2	200	85/20	~92	Dynamic
[60]	Receiver-side buck converter	Passivity-based PI control	Output power and efficiency	2.63	200	85/20	91.06	Dynamic
This work	Receiver-side active bridge	Pulse density control	Output power, voltage, and current	3.3	150	85	93.4	Dynamic

## 5. Economic Aspects of Multi-Transmitter Quasi-Dynamic Charging Lane

The quasi-dynamic wireless charging system reduces the cost of EVs effectively by reducing the volume of the battery and modifying the vehicle dynamics. Figure 25 illustrates the cost distribution of the proposed quasi-dynamic wireless charging system. The significant cost contributors of the charging lanes are power converters, resonant networks, power converters, and charging couplers. The proposed charging system utilizes the segmented multi-transmitter charging lane, which is energized by multi-legged inverter topology. The geometry of the DD-shaped charging coupler is  $70 \times 35$  (in cm), and it is embedded in the ground to transmit the energy. The optimal distance between the consecutive transmitters and its effective energization by the multi-legged inverter reduces the initial charging system's infrastructure cost-efficiently. The charging lane cost analysis is investigated for different km values with the cost of a five-legged inverter-driven LCC-driven four-transmitter pad charging system. The total cost of the charging system is the summation of the cost of power converters, resonant networks, charging pads, and controllers. The laboratory prototype was developed, and the component purchase price list is in Indian rupees (INR). The cost of the charging lane is mentioned in USD for the purpose of clarity. Though the initial infrastructure cost of the quasi-dynamic charging lane is high, it effectively reduces the vehicle's battery cost. Furthermore, this on-road charging system has a roadside charging track, and it does not require separate land in acres to develop the EV charging infrastructure.

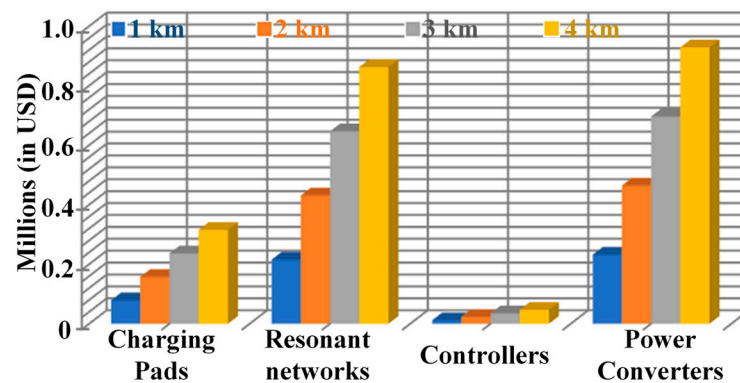


Figure 25. Cost distribution of the proposed quasi-dynamic charging lane.

## 6. Conclusions

The dynamic wireless charging system for EVs motivates the development of the sustainable transportation sector. The charging system reduces the heavy-volume battery requirements of EVs and extends the driving range of the EVs with an on-road charging system. The reduction in charging device ratings also reduces the demand for base materials of the battery system. The on-road wireless charging system eliminates the requirement of heavy gauge conductors to charge the batteries. The above-mentioned merits improve the reliability of the EV charging infrastructure. The article presented a quasi-dynamic wireless charging system for a slow-moving electric vehicle that regulates output parameters such as power, voltage, and current. The proposed system addresses the significant concerns of the quasi-dynamic wireless charging system such as load-independent constant charging, output power regulation, and output ripple reduction. A receiver-side active bridge rectifier regulates the output power using a pulse density-modulated technique. By modulating the pulse density of the controlling pulses, the output power of the battery system can be modified. The reconfigurable hybrid resonant network on the receiver side controls and regulates the output current and voltage, ensuring a constant magnitude regardless of the load variations. The LCC–SP configuration delivers a constant voltage, whereas the LCC–LCC configuration delivers a constant current. The combination of PDM-driven active bridge rectifiers and reconfigurable resonant networks ensures constant charging and power flow regulation. The SiC-based five-legged inverter is employed on the transmitter side to excite the four consecutive transmitters. The controller drives the inverter with respect to the predefined range of velocity. The inverter excites the corresponding transmitter pad when the receiver pad moves over it at a particular predefined velocity. The various ranges of power regulation are also ensured by the receiver-side active bridge rectifier with adjustable pulse density. The proposed topology enhances the charging system's overall performance.

**Author Contributions:** Methodology, Y.S. and N.R.; Validation, R.A. and A.A.; Investigation, N.R.; Resources, R.A.; Writing—original draft, Y.S.; Writing—review & editing, N.R. and A.A.; Supervision, R.A.; Funding acquisition, A.A. All authors have read and agreed to the published version of the manuscript.

**Funding:** This research was funded by Taif University, Taif, Saudi Arabia (TU-DSPP-2024-17). This work was supported in part by the Government of India, Department of Science and Technology (DST) Science and Engineering Research Board (SERB) Core Research Grant CRG/2020/004073.

**Institutional Review Board Statement:** Not applicable.

**Informed Consent Statement:** Not applicable.

**Data Availability Statement:** The data presented in this study are available on request from the corresponding author.

**Acknowledgments:** The author extend their appreciation to Taif University, Saudi Arabia, for supporting this work through project number (TU-DSPP-2024-17).

**Conflicts of Interest:** The authors declare no conflicts of interest.

## References

- Global EV Outlook 2022—Analysis—IEA. Available online: <https://www.iea.org/reports/global-ev-outlook-2022> (accessed on 10 January 2024).
- Xue, Y.; Zhang, X.; Zhang, Y.; Luo, E. Understanding the Barriers to Consumer Purchasing of Electric Vehicles: The Innovation Resistance Theory. *Sustainability* **2024**, *16*, 2420. [CrossRef]
- Liu, Z.; Wu, Y.; Feng, J. Competition between battery switching and charging in electric vehicle: Considering anticipated regret. *Environ. Dev. Sustain.* **2023**. [CrossRef]
- Hou, M.; Zhao, Y.; Ge, X. Optimal scheduling of the plug-in electric vehicles aggregator energy and regulation services based on grid to vehicle. *Int. Trans. Electr. Energy Syst.* **2017**, *27*, e2364. [CrossRef]
- Venkatesan, R.; Dominic Savio, A.; Balaji, C.; Narayanamoorthi, R.; Kotb, H.; ELrashidi, A.; Nureldeen, W. A Comprehensive Review on Efficiency Enhancement of Wireless Charging System for an Electric Vehicles Applications. *IEEE Access* **2024**, *12*, 46967–46994. [CrossRef]
- Shirkhani, M.; Tavooosi, J.; Danyali, S.; Sarvenoe, A.K.; Abdali, A.; Mohammadzadeh, A.; Zhang, C. A review on microgrid decentralized energy/voltage control structures and methods. *Energy Rep.* **2023**, *10*, 368–380. [CrossRef]
- Duan, Y.; Zhao, Y.; Hu, J. An initialization-free distributed algorithm for dynamic economic dispatch problems in microgrid: Modeling, optimization and analysis. *Sustain. Energy Grids Netw.* **2023**, *34*, 101004. [CrossRef]
- Li, P.; Hu, J.; Qiu, L.; Zhao, Y.; Ghosh, B.K. A Distributed Economic Dispatch Strategy for Power–Water Networks. *IEEE Trans. Control. Netw. Syst.* **2022**, *9*, 356–366. [CrossRef]
- Arif, S.M.; Lie, T.T.; Seet, B.C.; Ayyadi, S.; Jensen, K. Review of Electric Vehicle Technologies, Charging Methods, Standards and Optimization Techniques. *Electronics* **2021**, *10*, 1910. [CrossRef]
- Lu, L.; Wu, W.; Gao, Y.; Pan, C.; Yu, X.; Zhang, C.; Jin, Z. Study on current discrepancy and redistribution of HTS non-insulation closed-loop coils during charging/discharging and subsequent transient process toward steady-state operation. *Supercond. Sci. Technol.* **2022**, *35*, 095001. [CrossRef]
- Zhang, X.; Wang, Z.; Lu, Z. Multi-objective load dispatch for microgrid with electric vehicles using modified gravitational search and particle swarm optimization algorithm. *Appl. Energy* **2022**, *306*, 118018. [CrossRef]
- Zhang, X.; Lu, Z.; Yuan, X.; Wang, Y.; Shen, X. L2-Gain Adaptive Robust Control for Hybrid Energy Storage System in Electric Vehicles. *IEEE Trans. Power Electron.* **2021**, *36*, 7319–7332. [CrossRef]
- Liang, J.; Feng, J.; Fang, Z.; Lu, Y.; Yin, G.; Mao, X.; Wu, J.; Wang, F. An Energy-Oriented Torque-Vector Control Framework for Distributed Drive Electric Vehicles. *IEEE Trans. Transp. Electrification* **2023**, *9*, 4014–4031. [CrossRef]
- Lyu, W.; Hu, Y.; Liu, J.; Chen, K.; Liu, P.; Deng, J.; Zhang, S. Impact of battery electric vehicle usage on air quality in three Chinese first-tier cities. *Sci. Rep.* **2024**, *14*, 21. [CrossRef] [PubMed]
- Purushothaman, D.; Narayanamoorthi, R.; Elrashidi, A.; Kotb, H. A Comprehensive Review on Single-Stage WPT Converter Topologies and Power Factor Correction Methodologies in EV Charging. *IEEE Access* **2023**, *11*, 135529–135555. [CrossRef]
- Alternative Fuels Data Center: Developing Infrastructure to Charge Electric Vehicles. Available online: [https://afdc.energy.gov/fuels/electricity\\_infrastructure.html](https://afdc.energy.gov/fuels/electricity_infrastructure.html) (accessed on 11 January 2024).
- Zhang, X.; Wang, Y.; Yuan, X.; Shen, Y.; Lu, Z.; Wang, Z. Adaptive Dynamic Surface Control with Disturbance Observers for Battery/Supercapacitor-Based Hybrid Energy Sources in Electric Vehicles. *IEEE Trans. Transp. Electrification* **2023**, *9*, 5165–5181. [CrossRef]
- Fang, Z.; Wang, J.; Liang, J.; Yan, Y.; Pi, D.; Zhang, H.; Yin, G. Authority Allocation Strategy for Shared Steering Control Considering Human-Machine Mutual Trust Level. *IEEE Trans. Intell. Veh.* **2024**, *9*, 2002–2015. [CrossRef]
- Bai, X.; Xu, M.; Li, Q.; Yu, L. Trajectory-battery integrated design and its application to orbital maneuvers with electric pump-fed engines. *Adv. Space Res.* **2022**, *70*, 825–841. [CrossRef]
- Ahmad, F.; Alam, M.S.; Alsaidan, I.S.; Shariff, S.M. Battery Swapping Station for Electric Vehicles: Opportunities and Challenges. *IET Smart Grid* **2020**, *3*, 280–286. [CrossRef]
- Ahmad, F.; Alam, M.S.; Shariff, S.M. A Cost-Efficient Energy Management System for Battery Swapping Station. *IEEE Syst. J.* **2019**, *13*, 4355–4364. [CrossRef]
- Lu, X.; Wang, P.; Niyato, D.; Kim, D.I.; Han, Z. Wireless Charging Technologies: Fundamentals, Standards, and Network Applications. *IEEE Commun. Surv. Tutor.* **2016**, *18*, 1413–1452. [CrossRef]
- Farh, H.M.H.; Fathy, A.; Iqbal, S.; Alshammari, N.F.; Shouran, M.; Massoud, J. Smart and Sustainable Wireless Electric Vehicle Charging Strategy with Renewable Energy and Internet of Things Integration. *Sustainability* **2024**, *16*, 2487. [CrossRef]
- Ahmad, A.; Alam, M.S.; Chabaan, R. A Comprehensive Review of Wireless Charging Technologies for Electric Vehicles. *IEEE Trans. Transp. Electrification* **2017**, *4*, 38–63. [CrossRef]
- Shanmugam, Y.; Narayanamoorthi, R.; Vishnuram, P.; Bajaj, M.; Aboras, K.M.; Thakur, P. Kitmo A Systematic Review of Dynamic Wireless Charging System for Electric Transportation. *IEEE Access* **2022**, *10*, 133617–133642. [CrossRef]

26. Li, C.; Dong, X.; Cipcigan, L.M.; Haddad, M.A.; Sun, M.; Liang, J.; Ming, W. Economic Viability of Dynamic Wireless Charging Technology for Private EVs. *IEEE Trans. Transp. Electrification*. **2022**, *9*, 1845–1856. [[CrossRef](#)]
27. Bozhi; Mohamed, M.; Gilani, V.N.M.; Amjad, A.; Majid, M.S.; Yahya, K.; Salem, M. A Review of Wireless Pavement System Based on the Inductive Power Transfer in Electric Vehicles. *Sustainability* **2023**, *15*, 14893. [[CrossRef](#)]
28. Tavakoli, R.; Dede, E.M.; Chou, C.; Pantic, Z. Cost-Efficiency Optimization of Ground Assemblies for Dynamic Wireless Charging of Electric Vehicles. *IEEE Trans. Transp. Electrification*. **2022**, *8*, 734–751. [[CrossRef](#)]
29. Cai, C.; Saeedifard, M.; Wang, J.; Zhang, P.; Zhao, J.; Hong, Y. A Cost-Effective Segmented Dynamic Wireless Charging System With Stable Efficiency and Output Power. *IEEE Trans. Power Electron.* **2022**, *37*, 8682–8700. [[CrossRef](#)]
30. Benalia, N.; Laroussi, K.; Benlaloui, I.; Kouzou, A.; Bensalah, A.-D.; Kennel, R.; Abdelrahman, M. Optimized Power Pads for Charging Electric Vehicles Based on a New Rectangular Spiral Shape Design. *Sustainability* **2023**, *15*, 1230. [[CrossRef](#)]
31. Rahulkumar, J.; Narayanamoorthi, R.; Vishnuram, P.; Bajaj, M.; Blazek, V.; Prokop, L.; Misak, S. An Empirical Survey on Wireless Inductive Power Pad and Resonant Magnetic Field Coupling for In-Motion EV Charging System. *IEEE Access* **2023**, *11*, 4660–4693. [[CrossRef](#)]
32. Yuvaraja, S.; Narayanamoorthi, R.; Sathik Mohamed Ali, J.; Almakhles, D. A Comprehensive Review of the On-Road Wireless Charging System for E-Mobility Applications. *Front. Energy Res.* **2022**, *10*, 926270. [[CrossRef](#)]
33. Zaheer, A.; Hao, H.; Covic, G.A.; Kacprzak, D. Investigation of Multiple Decoupled Coil Primary Pad Topologies in Lumped IPT Systems for Interoperable Electric Vehicle Charging. *IEEE Trans. Power Electron.* **2015**, *30*, 1937–1955. [[CrossRef](#)]
34. Budhia, M.; Boys, J.T.; Covic, G.A.; Huang, C.-Y. Development of a Single-Sided Flux Magnetic Coupler for Electric Vehicle IPT Charging Systems. *IEEE Trans. Ind. Electron.* **2013**, *60*, 318–328. [[CrossRef](#)]
35. Villa, J.L.; Sallan, J.; Osorio, J.F.S.; Llombart, A. High-Misalignment Tolerant Compensation Topology for ICPT Systems. *IEEE Trans. Ind. Electron.* **2012**, *59*, 945–951. [[CrossRef](#)]
36. Zhang, W.; Mi, C.C. Compensation Topologies of High-Power Wireless Power Transfer Systems. *IEEE Trans. Veh. Technol.* **2016**, *65*, 4768–4778. [[CrossRef](#)]
37. Shevchenko, V.; Husev, O.; Strzelecki, R.; Pakhaliuk, B.; Poliakov, N.; Strzelecka, N. Compensation Topologies in IPT Systems: Standards, Requirements, Classification, Analysis, Comparison and Application. *IEEE Access* **2019**, *7*, 120559–120580. [[CrossRef](#)]
38. Chowdary, K.V.; Kumar, K.; Behera, R.K.; Banerjee, S.; Kumar, R.R. Load Independent Characteristics of Dynamic Wireless Charging System through Higher Order Compensation. In Proceedings of the 9th IEEE International Conference on Power Electronics, Drives and Energy Systems (PEDES), Jaipur, India, 16–19 December 2020; pp. 1–6.
39. He, L.; Wang, X.; Lee, C.-K. A Study and Implementation of Inductive Power Transfer System Using Hybrid Control Strategy for CC-CV Battery Charging. *Sustainability* **2023**, *15*, 3606. [[CrossRef](#)]
40. Chen, J.; Xu, J.; Zhang, Y.; Zhao, J.; Hou, J.; Wang, Y. Geometrical State-Plane-based Synchronous Rectification Scheme for LLC Converter in EVs. *IEEE Trans. Transp. Electrification*. [[CrossRef](#)]
41. Lu, J.; Zhu, G.; Lin, D.; Wong, S.-C.; Jiang, J. Load-Independent Voltage and Current Transfer Characteristics of High-Order Resonant Network in IPT System. *IEEE J. Emerg. Sel. Top. Power Electron.* **2019**, *7*, 422–436. [[CrossRef](#)]
42. Zhang, J.; Zhu, D.; Jian, W.; Hu, W.; Peng, G.; Chen, Y.; Wang, Z. Fractional Order Complementary Non-singular Terminal Sliding Mode Control of PMSM Based on Neural Network. *Int. J. Automot. Technol.* **2024**, *25*, 213–224. [[CrossRef](#)]
43. Shanmugam, Y.; Narayanamoorthi, R.; Dominic, S.A.; Balaji, C. A Multi-Leg Powered Constant Voltage On-Road Charging System with an LCC-S Compensation. In Proceedings of the ITEC-India 2023—5th International Transportation Electrification Conference: eAMRIT—Accelerating e-Mobility Revolution for India’s Transportation, Chennai, India, 13–15 December 2023; Institute of Electrical and Electronics Engineers Inc.: Piscataway, NJ, USA, 2023.
44. Rahulkumar, J.; Narayanamoorthi, R.; Balaji, C.; Savio, A. A Dual Receiver and Inherent CC-CV Operated WRIPT EV Charging System with High Misalignment Tolerance Couplers. In Proceedings of the ITEC-India 2023—5th International Transportation Electrification Conference: eAMRIT—Accelerating e-Mobility Revolution for India’s Transportation, Chennai, India, 13–15 December 2023; Institute of Electrical and Electronics Engineers Inc.: Piscataway, NJ, USA, 2023.
45. Lu, J.; Zhu, G.; Lin, D.; Zhang, Y.; Jiang, J.; Mi, C.C. Unified Load-Independent ZPA Analysis and Design in CC and CV Modes of Higher Order Resonant Circuits for WPT Systems. *IEEE Trans. Transp. Electrification*. **2019**, *5*, 977–987. [[CrossRef](#)]
46. Shen, Y.; Liu, D.; Liang, W.; Zhang, X. Current Reconstruction of Three-Phase Voltage Source Inverters Considering Current Ripple. *IEEE Trans. Transp. Electrification*. **2023**, *9*, 1416–1427. [[CrossRef](#)]
47. Alkasir, A.; Abdollahi, S.E.; Abdollahi, S.R.; Wheeler, P. Enhancement of Dynamic Wireless Power Transfer System by Model Predictive Control. *IET Power Electron.* **2022**, *15*, 67–79. [[CrossRef](#)]
48. Yang, Y.; Wei, X.; Yao, W.; Lan, J. Broadband electrical impedance matching of sandwiched piezoelectric ultrasonic transducers for structural health monitoring of the rail in-service. *Sens. Actuators A Phys.* **2023**, *364*, 114819. [[CrossRef](#)]
49. Diep, N.T.; Hiep, T.D.; Trung, N.K. Constant Current Charging and Transfer Efficiency Improvements for a Dynamic Wireless Charging System. *Eng. Technol. Appl. Sci. Res.* **2023**, *13*, 12320–12326. [[CrossRef](#)]
50. Balaji, C.; Venugopal, R.; Selvaraj, J.; Balasundaram, G.; Savio, A.D.; Lim, W.H. Design and Performance Study of LCC-LCC and LCC-S Compensation Network for Wireless Charging of EV Battery. In Proceedings of the ITEC-India 2023—5th International Transportation Electrification Conference: eAMRIT—Accelerating e-Mobility Revolution for India’s Transportation, Chennai, India, 13–15 December 2023; Institute of Electrical and Electronics Engineers Inc.: Piscataway, NJ, USA, 2023.

51. Liang, Y.; Sun, P.; Yang, G.; Sun, J.; Cai, J.; Wu, X.; Deng, Q. Analysis and Parameter Design for Input-Series Output-Series (ISOS) Multichannel Inductive Power Transfer System Considering Cross Coupling. *IEEE J. Emerg. Sel. Top. Power Electron.* **2024**, *12*, 2361–2376. [[CrossRef](#)]
52. Vu, V.-B.; Phan, V.-T.; Dahidah, M.; Pickert, V. Multiple Output Inductive Charger for Electric Vehicles. *IEEE Trans. Power Electron.* **2019**, *34*, 7350–7368. [[CrossRef](#)]
53. Farajizadeh, F.; Vilathgamuwa, D.M.; Jovanovic, D.; Jayathurathnage, P.; Ledwich, G.; Madawala, U. Expandable N-Legged Converter to Drive Closely Spaced Multitransmitter Wireless Power Transfer Systems for Dynamic Charging. *IEEE Trans. Power Electron.* **2020**, *35*, 3794–3806. [[CrossRef](#)]
54. He, H.; Liu, Y.; Wei, B.; Wu, X.; Jiang, B.; Wei, C. Efficiency Improvement for Multi-Parallel Inverters IPT System in Wide Power Range. In Proceedings of the PEAS 2021—2021 IEEE 1st International Power Electronics and Application Symposium, Shanghai, China, 12–15 November 2021; Conference Proceedings. Institute of Electrical and Electronics Engineers Inc.: Piscataway, NJ, USA, 2021.
55. Yuvaraja, S.; Narayanamoorthi, R. A Five Leg Converter with Multi-Transmitter for an In-Motion Charging System. *J. Phys. Conf. Ser.* **2022**, *2335*, 012054. [[CrossRef](#)]
56. Zhang, J.; Chen, Y.; Gao, Y.; Wang, Z.; Peng, G. Cascade ADRC Speed Control Base on FCS-MPC for Permanent Magnet Synchronous Motor. *J. Circuits Syst. Comput.* **2021**, *30*, 2150202. [[CrossRef](#)]
57. Shanmugam, Y.; Narayanamoorthi, R.; Vishnuram, P.; Savio, D.; Yadav, A.; Bajaj, M.; Nauman, A.; Khurshaid, T.; Kamel, S. Solar-Powered Five-Leg Inverter-Driven Quasi-Dynamic Charging for a Slow-Moving Vehicle. *Front. Energy Res.* **2023**, *11*, 1115262. [[CrossRef](#)]
58. Wang, C.; Chen, Z.; Zheng, H.; Yang, Q. Power Control Study of Dynamic Wireless Charging System Based on Resonant Point Switching. In Proceedings of the 2022 IEEE Transportation Electrification Conference and Expo, Asia-Pacific (ITEC Asia-Pacific), Haining, China, 28–31 October 2022; pp. 1–5.
59. Karakitsios, I.; Palaioyiannis, F.; Markou, A.; Hatzigiorgiouri, N.D. Optimizing the Energy Transfer, with a High System Efficiency in Dynamic Inductive Charging of EVs. *IEEE Trans. Veh. Technol.* **2018**, *67*, 4728–4742. [[CrossRef](#)]
60. Liu, J.; Liu, Z.; Su, H. Passivity-Based PI Control for Receiver Side of Dynamic Wireless Charging System in Electric Vehicles. *IEEE Trans. Ind. Electron.* **2022**, *69*, 783–794. [[CrossRef](#)]
61. Farajizadeh, F.; Vilathgamuwa, M.; Jayathurathnage, P.; Ledwich, G. Three-Legged Converter for Dynamic Wireless Power Transfer. In Proceedings of the IECON 2018—44th Annual Conference of the IEEE Industrial Electronics Society, Washington, DC, USA, 21–23 October 2018.
62. Tian, Y.; Tian, J.; Li, D.; Zhou, S. A Multiple Legs Inverter with Real Time-Reflected Load Detection Used in the Dynamic Wireless Charging System of Electric Vehicles. *Energies* **2018**, *11*, 1275. [[CrossRef](#)]
63. Rashid, M.H.; Muhammad, H. *Power Electronics: Devices, Circuits, and Applications*, 4th ed.; Pearson: London, UK, 2014; ISBN 978-0-273-76908-8.
64. Abdulfameed, M.; ElGhanam, E.; Osman, A.H.; Hassan, M.S. Design of a Misalignment-Tolerant Inductor-Capacitor-Capacitor-Compensated Wireless Charger for Roadway-Powered Electric Vehicles. *Sustainability* **2024**, *16*, 567. [[CrossRef](#)]
65. Li, S.; Li, W.; Deng, J.; Nguyen, T.D.; Mi, C.C. A Double-Sided LCC Compensation Network and Its Tuning Method for Wireless Power Transfer. *IEEE Trans. Veh. Technol.* **2015**, *64*, 2261–2273. [[CrossRef](#)]
66. Li, M.; Deng, J.; Chen, D.; Wang, W.; Wang, Z. Maximum Efficiency Tracking and ZVS Realization for Wide Output Voltage Range Employing Segmented TPS Modulation Scheme. *IEEE Trans. Veh. Technol.* **2023**, *72*, 12770–12783. [[CrossRef](#)]
67. Venkatesan, M.; Narayanamoorthi, R.; Emara, A.; Ghadi, Y.Y. Fuzzy Logic Controlled Pulse Density Modulation Technique for Bidirectional Inductive Power Transfer Systems. *IEEE Access* **2024**, *Early Access*. [[CrossRef](#)]
68. Zhang, B.; Dong, S.; Zhu, C.; Yin, Y.; Zhang, M. Composite Control to Suppress Output Fluctuation for Receiver Side of Dynamic Wireless Power Transfer System. *IEEE Trans. Power Electron.* **2023**, *38*, 6720–6733. [[CrossRef](#)]
69. Zhou, Z.; Zhang, L.; Liu, Z.; Chen, Q.; Long, R.; Su, H. Model Predictive Control for the Receiving-Side DC-DC Converter of Dynamic Wireless Power Transfer. *IEEE Trans. Power Electron.* **2020**, *35*, 8985–8997. [[CrossRef](#)]

**Disclaimer/Publisher’s Note:** The statements, opinions and data contained in all publications are solely those of the individual author(s) and contributor(s) and not of MDPI and/or the editor(s). MDPI and/or the editor(s) disclaim responsibility for any injury to people or property resulting from any ideas, methods, instructions or products referred to in the content.